J. Fluid Mech. (2020), *vol.* 889, A14. © The Author(s), 2020.
Published by Cambridge University Press
doi:10.1017/jfm.2020.53

A continuum-scale representation of Ostwald ripening in heterogeneous porous media

Yaxin Li[1],†, Charlotte Garing[2] and Sally M. Benson[1]

[1]Department of Energy Resources Engineering, Stanford University, Stanford, CA 94305, USA
[2]Department of Geology, University of Georgia, Athens, GA 30602, USA

(Received 13 June 2019; revised 20 November 2019; accepted 13 January 2020)

Ostwald ripening is a pore-scale phenomenon that coarsens a dispersed phase until thermodynamic equilibrium. Based on our previous finding that multi-bubble equilibrium is possible and likely in complex porous media, we develop a new continuum-scale model for Ostwald ripening in heterogeneous porous media. In this model, porous media with two different capillary pressure curves are put into contact, allowing only diffusive flow through the aqueous phase to redistribute a trapped gas phase. Results show that Ostwald ripening can increase the gas saturation in one medium while decreasing the gas saturation in the other, even when the gas phase is trapped in pore spaces by capillary forces. We develop an analogous retardation factor to show that the characteristic time for Ostwald ripening is about 10^5 times slower than a single-phase diffusion problem due to the fact that separate-phase gas requires a much larger amount of mass transfer before equilibrium is established. An approximate solution has been developed to predict the saturation redistribution between the two media. The model has been validated by numerical simulation over a wide range of physical parameters. Millimetre to centimetre-scale systems come to equilibrium in years, ranging up to 10 000 years and longer for metre-scale systems. These findings are particularly relevant for geological CO_2 storage, where residual trapping is an important mechanism for immobilizing CO_2. Our work demonstrates that Ostwald ripening due to heterogeneity in porous media is slow and on a similar time scale compared to other processes that redistribute trapped CO_2 such as convective mixing.

Key words: bubble dynamics, multiphase flow, porous media

1. Introduction

Ostwald ripening is a phase coarsening phenomenon that has been observed in various systems where a dispersed second phase is present (Greenwood 1956; Lifshitz & Slyozov 1961; Plesset & Sadhal 1982; Voorhees 1985, 1992). In a bulk liquid, the dispersed phase in the form of bubbles is coarsened by growth of large bubbles at

† Email address for correspondence: yaxinl@stanford.edu

the expense of small bubbles. Capillary pressure of a bubble can be expressed as a function of its radius according to Laplace's law, i.e.

$$P_c = \frac{2\sigma}{r}, \tag{1.1}$$

where P_c is the pressure difference between the two phases, σ is the interfacial tension and r is the interfacial radius. Coexistence of bubbles of different sizes leads to capillary pressure gradients within the system, serving as the driving force for Ostwald ripening. The mass fraction of dissolved gas species in the continuous phase adjacent to an interface is proportional to local capillary pressure according to Henry's law, i.e.

$$X = \frac{P_w + P_c}{H}, \tag{1.2}$$

where X is the mass fraction of dissolved gas species in the adjacent continuous phase, P_w is the pressure of the continuous phase and H is Henry's constant. This mass fraction gradient drives mass flux from the bubbles with high capillary pressure toward regions of low capillary pressure.

In a bulk liquid, the interfacial radius is equivalent to the bubble radius because the interface is spherical and can grow without spatial restriction. In a porous medium, however, the presence of a solid matrix adds complexity to the Ostwald ripening process. The shape of each individual ganglion is strongly restricted by local pore topography, and interfacial radii at free interfaces are strongly dependent on pore geometry (Bear 2013). Given the circumstances, capillary pressure of a ganglion is rather a complex function of local pore topography and pore size instead of its volume (Garing *et al.* 2017). This fact leads to difficulty when predicting mass redistribution of dispersed ganglia by Ostwald ripening due to capillary pressure gradients.

Past studies of Ostwald ripening in porous media have dealt with this complexity in a number of ways. For example, Ostwald ripening has been neglected because concentration gradients imposed by the rate of change of the supersaturation were significantly larger than those driving Ostwald ripening (Li & Yortsos 1995; Tsimpanogiannis & Yortsos 2002). Other studies on Ostwald ripening in porous media neglected capillary pressure gradients (Dominguez, Bories & Prat 2000; Goldobin & Brilliantov 2011). In recent years, Ostwald ripening in porous media driven by capillary pressure gradients has gained researchers' attention due to its potential application to geological carbon sequestration (Garing *et al.* 2017; Xu, Bonnecaze & Balhoff 2017; de Chalendar, Garing & Benson 2018). In particular, one important mechanism of immobilizing CO_2 is referred to as residual trapping, where injected CO_2 is residually trapped in the form of disconnected ganglia by capillary forces (Hesse, Orr & Tchelepi 2008; Bear 2013). If residual CO_2 ganglia coexist at different capillary pressures, the resulting capillary pressure gradients will initiate Ostwald ripening. Consequently, ganglia may shrink or grow resulting in redistribution of residual CO_2 and potentially, re-aggregation of initially disconnected CO_2.

To evaluate the potential for Ostwald ripening in porous media, it is necessary to determine the capillary pressure of a single ganglion. Andrew, Bijeljic & Blunt (2014) imaged trapped CO_2 ganglia in a limestone sample at reservoir conditions and calculated curvatures of CO_2–brine interfaces. The measured curvatures over a single ganglion display a well-defined peak, indicating that a single ganglion is present at a single value of capillary pressure. This observation is also supported by an analysis on interfacial curvatures in an air–brine system performed by Garing *et al.* (2017).

In addition to a single ganglion, studies have shown that a group of adjacent ganglia can reach local capillary equilibrium. de Chalendar *et al.* (2018) developed a pore-network model for simulating Ostwald ripening accounting for capillary effects using conically-shaped pore throats. The authors demonstrated that CO_2 ganglia across several pores with initially different capillary pressures could eventually approach capillary equilibrium by inter-ganglion diffusion on the time scale of years. This finding was supported by a two-and-a-half-dimensional micro-model experiment (Xu *et al.* 2017), where the authors reported that trapped gas ganglia with initially different sizes can eventually approach a uniform size. Furthermore, Garing *et al.* (2017) showed that the equilibrium capillary pressure of trapped air ganglia is roughly at the same order of the entry pressure of the porous medium. This observation implied that not only is there a potential for Ostwald ripening among local ganglia across several pores, but also among the groups of ganglia in porous media with different entry pressures.

The above findings of Garing *et al.* (2017) and de Chalendar *et al.* (2018) give rise to a new scenario of Ostwald ripening in the context of geological CO_2 sequestration. Supercritical CO_2 is injected into a reservoir and forms a CO_2 plume that flows laterally and upward driven by viscous and buoyancy forces. After injection stops, reservoir water imbibes into the CO_2 plume and traps CO_2 in the form of residual CO_2. Residually trapped CO_2 could reach local capillary equilibrium rapidly at the same order of the local entry pressure. Capillary heterogeneity can be observed at various spatial scales above the representative elementary volume (REV) such as from the sub-core scale to the reservoir scale and results in variation of local entry pressure (Van Genuchten 1980; Pini, Krevor & Benson 2012). Therefore, different sections of a heterogeneous reservoir have different capillary pressure curves. These capillary pressure gradients can initiate Ostwald ripening among locally equilibrated residually trapped CO_2 and may result in CO_2 redistribution in the reservoir even though the CO_2 ganglia are completely trapped. Therefore, it is crucial to evaluate the impact of Ostwald ripening in this scenario on residual CO_2 and evaluate the time scale for redistribution, owing to the fact that redistribution may re-aggregate disconnected CO_2 and remobilize the trapped CO_2.

To this end, we investigate the consequences of Ostwald ripening on the equilibrium of residually trapped CO_2 driven by reservoir heterogeneity. Three contributions are made in this paper. Firstly, we use a continuum-scale multi-physics numerical model to demonstrate redistribution of residually trapped CO_2 by Ostwald ripening. Secondly, we develop an analogous retardation factor based on the mathematical model of Ostwald ripening to compare the time scale of capillary equilibrium to that of single-phase diffusion. Lastly, we develop a new approximate solution for predicting the redistribution of residually trapped CO_2 over the entire course of evolution, serving as a tool to evaluate the importance of Ostwald ripening at various spatial scales and over a wide range of reservoir properties and initial conditions.

2. Continuum-scale numerical simulation of Ostwald ripening

2.1. *The conceptual model*

The conceptual model underlying this work is defined by re-equilibration between several adjacent domains of residual CO_2 ganglia that are locally equilibrated within each domain, but are out of capillary equilibrium with the adjacent domains. During the re-equilibration period, residual CO_2 redistributes between the domains by diffusion of CO_2 through the aqueous phase, causing the capillary pressures of

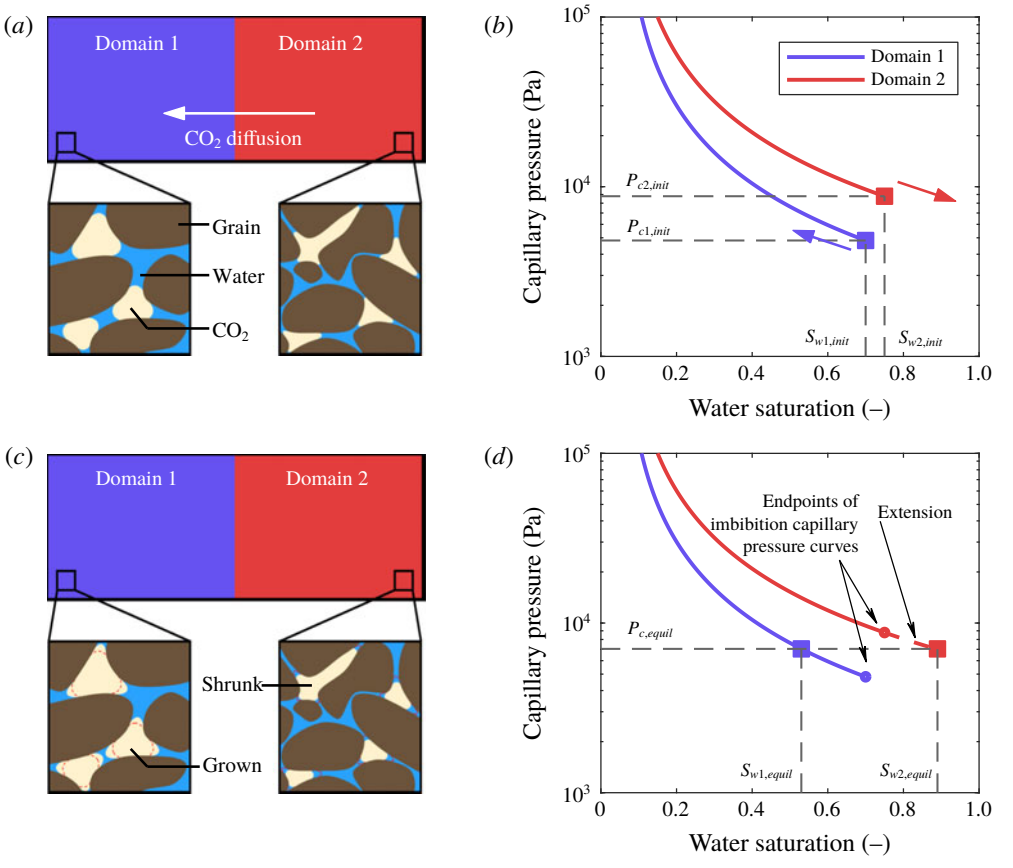

FIGURE 1. A continuum-scale conceptual representation of Ostwald ripening of residually trapped CO_2. (*a*) An illustration of the initial condition. The CO_2 ganglia are trapped in pore spaces and at local capillary equilibrium. Their interfacial curvatures are uniform within a domain and different between domains. (*b*) Capillary pressure distribution at the initial condition. The initial condition is at the end of imbibition where capillary pressures of residual CO_2 are represented by the endpoints of imbibition capillary pressure curves. (*c*) An illustration at equilibrium. Trapped CO_2 ganglia shrink or grow due to Ostwald ripening, and their interfacial curvatures approach the same value between domains. (*d*) Capillary pressure distribution at equilibrium. The CO_2 saturation within the two domains redistributes due to Ostwald ripening and approach capillary equilibrium between domains.

all domains to eventually approach the same value. When the spatial scale that ganglia groups expand over is above the REV, this pore-scale phenomenon manifests its effects at the continuum scale, where residual CO_2 saturation changes among domains. Here, we develop a continuum-scale model to link this redistribution to its pore-scale origins.

This model focuses on the supercritical CO_2–water system, but could equally well be used for other pairs of immiscible fluids. The model is horizontal and one-dimensional with closed boundaries and consist of two domains. As shown in figure 1(*a*), the two domains are homogeneous respectively, while their capillary pressure curves are different as shown in figure 1(*b*). The two domains are connected

to allow the aqueous phase to move freely between them so that the pressure in the aqueous phase is the same across the entire model.

The initial condition for this model is assumed to be shortly after imbibition, after pore-scale capillary equilibrium of the ganglia within each domain has been established, as shown in figure 1(*b*). The CO_2 is assumed to be completely immobile with zero relative permeability at any saturation. The capillary pressure of the trapped CO_2 is assumed to be slightly above the entry pressure of the rock, as found in Garing *et al.* (2017). The capillary pressure gradient between the two domains creates a CO_2 mass fraction gradient in the aqueous phase to drive CO_2 to diffuse from the high capillary pressure domain to the low capillary pressure domain. The saturation of CO_2 within the two domains redistributes during equilibration, and the two capillary pressures eventually approach equilibrium, as shown in figure 1(*c,d*).

We simply choose two imbibition capillary pressure curves to link residual CO_2 saturation to capillary pressure for each domain. In the high capillary pressure domain, capillary pressure will decrease as it equilibrates with the other domain. We assume that this decrease in capillary pressure follows an extension of the imbibition curve, as shown in figure 1(*d*). The extension fulfils two requirements. Firstly, capillary pressure should decrease as CO_2 ganglia retreat from the pore throats towards the pore body. Secondly, the capillary pressure curve should not fall below the entry pressure of the rock. For the low capillary pressure domain, the capillary pressure will increase as Ostwald ripening occurs. We assume that during this period, the capillary pressure will follow the imbibition curves shown in figure 1(*b*). It should be noted that the imbibition capillary pressure curves chosen here only describe the mathematical relationship between residual CO_2 saturation and its capillary pressure instead of indicating the process to be imbibition. Conventionally, capillary pressure hysteresis only applies to the continuous non-wetting phase, and the residual non-wetting phase is excluded from the measurement of capillary pressure (Bear 2013). Therefore, we do not adopt the concept of hysteresis to describe the capillary pressure change for residual CO_2 due to Ostwald ripening, and choosing imbibition curves is only for convenience as it represents a reasonable trend. The actual capillary pressure changes due to continuum-scale Ostwald ripening of residually trapped CO_2 could, in principle, be acquired by measuring the interfacial curvature through micro-CT imaging, although the long time scales would make this very challenging (Garing *et al.* 2017).

2.2. *Description of the numerical model*

The numerical simulator used for this problem is TOUGH2, a widely used simulator in problems relevant to flow in porous media such as geological CO_2 sequestration and nuclear waste disposal (Pruess, Oldenburg & Moridis 1999). The equation-of-state ECO2N is adopted to describe the thermodynamic properties of CO_2–water–NaCl systems. This equation-of-state reproduces mutual solubility in the CO_2–brine system within experimental accuracy and covers a wide range of temperatures (10–110 °C), pressure ($\leqslant$ 600 bar) and salinity (up to full halite saturation) (Spycher & Pruess 2005; Pruess & Spycher 2007).

The model is horizontal and one-dimensional with two equal-length domains as shown in figure 1 with two closed boundaries. Each domain is discretized into 8 grid cells of equal size, for a total of 16 grid cells in the model. The closed boundaries on the left- and right-hand side of the model can be interpreted as the region around the connection between two domains in a periodic heterogeneous system. The initial

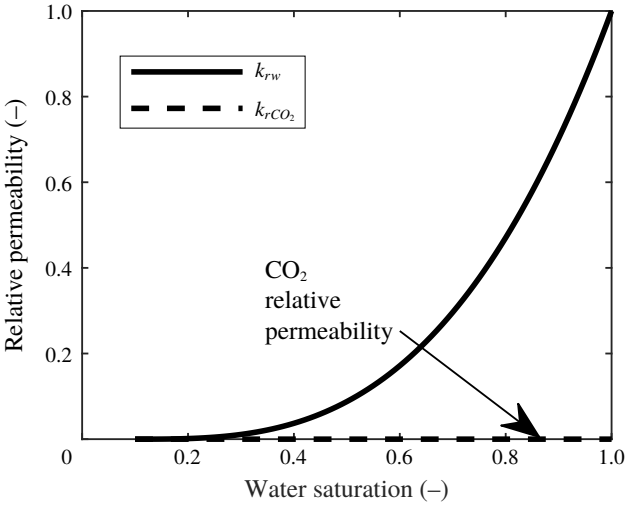

FIGURE 2. An example of the relative permeability model used in the conceptual model and numerical simulation. The CO_2 relative permeability is set to 0 at all saturation to ensure that separate-phase CO_2 is immobile over the entire course of evolution.

condition assumes the presence of a completely trapped residual CO_2 phase within each domain. As shown in figure 2, the relative permeability of the CO_2 phase is set to be zero over the entire saturation range, which ensures that the CO_2 phase stays immobile no matter how the saturation changes. In principle, the CO_2 phase may become mobile when its saturation increases. However, for this study we choose to investigate the particular case where the separate-phase CO_2 remains immobile to isolate the effects of Ostwald ripening on the non-wetting phase redistribution. Future work will explore the implications of remobilizing the CO_2 phase.

The two domains are assigned two different capillary pressure curves. The relative permeability and the capillary pressure characteristic curves are provided in table 1. These models and their parameters are picked because they represent experimentally measured properties of sandstone (Krevor *et al.* 2012). In addition, these models are flexible enough to adjust the curve characteristics such as entry pressure, irreducible saturation and curve steepness to represent a wide variety of rock types.

One example case is set up with its input parameters in table 1. For the full set of simulations, the input parameters are randomly generated within the ranges that are representative of typical reservoir conditions and reservoir properties for geological CO_2 sequestration. For the initial condition, the residual CO_2 within each domain is at local capillary equilibrium, resulting in a sharp gradient initially at the boundary between the two domains.

2.3. *Results of numerical simulation*

Results from the example case of the numerical simulation are presented in figure 3. During the early stages, a sharp gradient of CO_2 capillary pressure and resulting CO_2 mass fraction gradient can be seen at the interface between the two domains. Here, the CO_2 mass fraction in the aqueous phase X is defined as

$$X = \frac{\text{mass of dissolved } CO_2}{\text{mass of dissolved } CO_2 + \text{mass of water}}. \tag{2.1}$$

Category	Parameter	Domain 1	Domain 2	Unit	Description
Rock property	k	1.08×10^{-13}	5.62×10^{-14}	m^2	Permeability
	ϕ	0.165	0.198	—	Porosity
Capillary pressure model	$P_c = P_e + P_0 \left(\frac{1 - S_w}{S_w - S_{wi}} \right)^{1/\lambda}$				Narasimhan *et al.* (1978)
	P_e	3063	4248	Pa	Entry pressure
	P_0	7659	10621	Pa	Fitting parameter 1
	λ	0.78	0.78	—	Fitting parameter 2
	S_{wi}	0.04	0.04	—	Irreducible water
Relative permeability model	$k_{rw} = S^3,\ k_{rCO_2} = 0,\ where\ S = \frac{S_w - S_{wi}}{1 - S_{wi}}$				Verma *et al.* (1985)
Domain size	$L/2$	0.005	0.005	m	Domain length
Initial condition	P_w	13.9		MPa	Reservoir pressure
	T	70		°C	Temperature
	D_w	5.04×10^{-9}		$m^2\ s^{-1}$	Diffusion coefficient of CO_2 in the aqueous phase (Cadogan *et al.* 2014)

TABLE 1. Simulation input parameters of the example case shown in figure 3.

This mass fraction gradient initiates diffusion of CO_2 in the aqueous phase from the high capillary pressure domain to the other. Over time, the gradients of CO_2 mass fraction and capillary pressure decrease, and CO_2 saturation redistributes between the two domains even though the separate-phase CO_2 is set to be immobile over the entire simulation period (e.g. the relative permeability is zero). The results show that Ostwald ripening is capable of changing the saturation distribution of CO_2 between the two domains.

For the example shown here, establishing equilibrium between the two domains requires a period of about 10 years, even though the domain size is very small (0.01 m).

3. Mathematical model for residual CO_2 redistribution by Ostwald ripening

Numerical simulation shows that residual CO_2 can be redistributed by Ostwald ripening even though the residual CO_2 is completely immobile. However, the redistribution by Ostwald ripening is extremely slow. The characteristic time for diffusion is usually expressed as

$$t_c = \frac{l^2}{D}, \tag{3.1}$$

where l is the characteristic length of the model and D is the diffusion coefficient. For a single-phase diffusion problem (only the aqueous phase and dissolved CO_2) with the same size of the numerical model shown in the last section, the characteristic time should be of the order of hours. However, the time to approach equilibrium

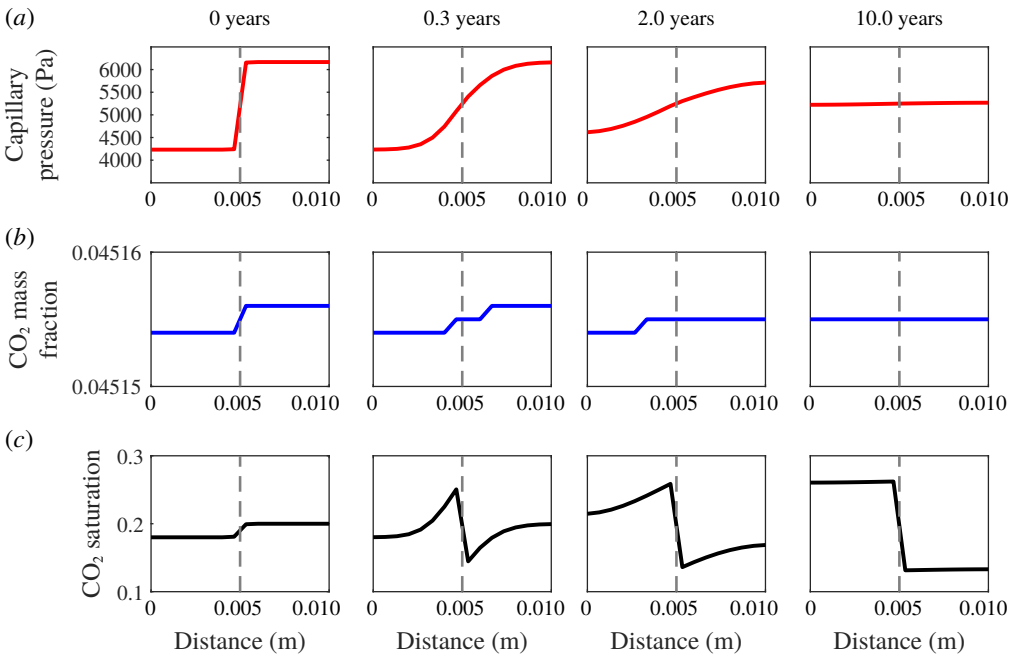

FIGURE 3. An example of numerical simulation on redistributing residually trapped CO_2 by Ostwald ripening in the aqueous phase. The evolution of (*a*) capillary pressure, (*b*) CO_2 mass fraction in the aqueous phase and (*c*) CO_2 saturation are shown. The CO_2 saturation increases in the low capillary pressure domain due to Ostwald ripening even though the separate-phase CO_2 is immobile.

for Ostwald ripening is about 10 years. In this section, we develop a mathematical model to explain the large difference between the single-phase diffusion problem and the Ostwald ripening problem. This model is expected to provide insights on the retardation of the equilibration, and assumptions will be made in this model to reduce complexity such as reducing variables to constants that have little impacts on the diffusion problem.

As shown in figure 1, the low capillary pressure domain (domain 1) is receiving the diffusive flux of CO_2 from the high capillary pressure domain (domain 2). The diffusive flux is responsible for both the increase of CO_2 mass fraction in the aqueous phase and the growth of separate-phase CO_2. By assuming diffusion only, without any advection of the CO_2 phase, the mass conservation equation for CO_2 is

$$\frac{\partial (XS_w\rho_w\phi)}{\partial t} + \frac{\partial (YS_g\rho_g\phi)}{\partial t} = \frac{\partial}{\partial x}\left[\phi D_w S_w \frac{\partial (X\rho_w)}{\partial x}\right], \tag{3.2}$$

where X and Y are the CO_2 mass fractions in the aqueous phase and in the CO_2 phase, respectively, S_w and S_g are the water saturation and CO_2 saturation, ρ_w and ρ_g are the water density and CO_2 density, and x is the distance. The term $\phi D_w S_w$ can be viewed as the effective diffusion coefficient accounting for the area open to diffusion.

Equation (3.2) can be simplified by assuming some variables are constants. First, the water density ρ_w, CO_2 density ρ_g, diffusion coefficient D_w and porosity ϕ can be assumed constant and equal to the values in domain 2 due to constant temperature and

a negligible change of pressure during the evolution compared to reservoir pressure. Second, the CO_2 mass fraction in the gaseous phase Y can be assumed to be equal to 1. Although Y is a complex function of X and local reservoir conditions as shown in equations 1 and 2 in Spycher & Pruess (2005), figure 2 of their paper shows that the water mole fraction in the CO_2 phase is near 1 %–2 % for reservoir conditions. Therefore, Y can be expected to be larger than 99 %. Third, water saturation can be assumed to be 1 for simplicity. The first and second terms in (3.2) represent the CO_2 mass in the aqueous phase and in the CO_2 phase, respectively. Considering Y (around 99 %) is much larger than X (around 5 %) (Spycher & Pruess 2005) and there is a high saturation of residual CO_2 (Burnside & Naylor 2014), the amount of CO_2 in the aqueous phase is significantly smaller than that in the CO_2 phase. Therefore, it is safe to assume that $S_w = 1$ with minimal impact on the total amount of CO_2 in the system. Based on the above assumptions, equation (3.2) becomes

$$\frac{\partial X}{\partial t} + \frac{\rho_g}{\rho_w}\frac{\partial S_g}{\partial t} = D_w \frac{\partial^2 X}{\partial x^2}. \tag{3.3}$$

Changes in S_g can be expressed as a function of changes in local CO_2 mass fraction X by

$$\frac{\partial S_g}{\partial t} = \frac{\mathrm{d}S_g}{\mathrm{d}P_c}\frac{\mathrm{d}P_c}{\mathrm{d}X}\frac{\partial X}{\partial t}. \tag{3.4}$$

In (3.4) the term $\mathrm{d}S_g/\mathrm{d}P_c$ can be calculated from the capillary pressure model for the rock. The term $\mathrm{d}P_c/\mathrm{d}X$ can be estimated based on the data from Spycher & Pruess (2005) for specific reservoir conditions. Detailed estimation of this term will be described in the following section.

Substituting (3.4) into (3.3), equation (3.3) can be written in the form

$$R_{CO_2}\frac{\partial X}{\partial t} = D_w \frac{\partial^2 X}{\partial x^2}, \tag{3.5}$$

where

$$R_{CO_2} = 1 + \frac{\rho_g}{\rho_w}\frac{\mathrm{d}S_g}{\mathrm{d}P_c}\frac{\mathrm{d}P_c}{\mathrm{d}X}. \tag{3.6}$$

Here, R_{CO_2} is analogous to the concept of the 'retardation factor' commonly used in convection–dispersion problems with absorptive materials where the advance of the solute is retarded due to adsorption of the solute onto the matrix (Bear 2013). The term $(\rho_g/\rho_w)(\mathrm{d}S_g/\mathrm{d}P_c)(\mathrm{d}P_c/\mathrm{d}X)$ is equivalent to the 'adsorption' term that retards the progress of CO_2 diffusion in the aqueous phase by absorbing CO_2 into the CO_2 phase. The time scale of residual CO_2 redistribution by Ostwald ripening can be estimated based on the time scale of the retarded diffusion process, such as the magnitude of R_{CO_2}.

To summarize, the mathematical model of residual CO_2 distribution by Ostwald ripening can be expressed by re-arranging equation (3.5) to give

$$\frac{\partial X}{\partial t} = D_{equiv}\frac{\partial^2 X}{\partial x^2}, \tag{3.7}$$

with the equivalent diffusion coefficient

$$D_{equiv} = \frac{D_w}{R_{CO_2}}. \tag{3.8}$$

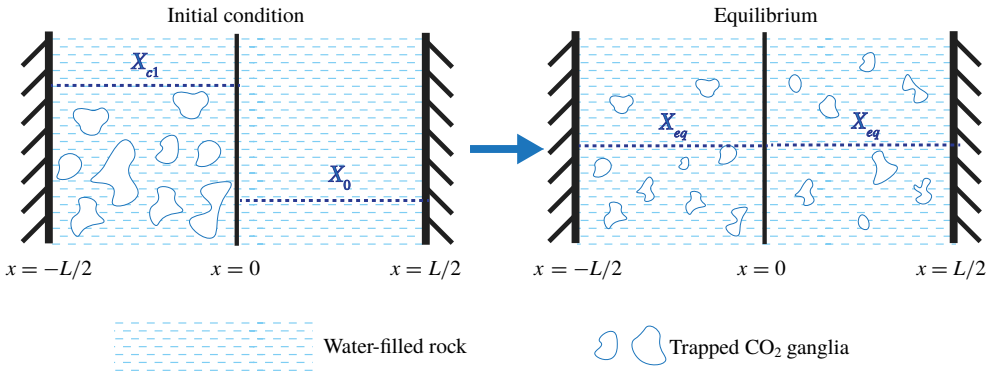

FIGURE 4. A conceptual illustration of a homogeneous case with a CO_2-saturated aqueous phase and only one domain initially containing separate-phase CO_2. The system approaches equilibrium through diffusive flux of CO_2 in the aqueous phase transporting CO_2 to increase CO_2 saturation in the other domain. Eventually, the CO_2 saturation will approach the same at equilibrium.

4. Exact solution for Ostwald ripening in a homogeneous system and characteristic time

4.1. *Exact solution for Ostwald ripening in a homogeneous system*

Equations in the form of (3.7) have been solved extensively for particular representations of D_{equiv} (Fokas & Yortsos 1982; Kashchiev & Firoozabadi 2003). However, the problem we are interested in for this paper is defined as a two-domain system with different capillary pressure curves in each domain. This situation may cause the term $\mathrm{d}S_g/\mathrm{d}P_c$ in the diffusion coefficient to be in nonlinear and discontinuous forms that make the differential equation non-solvable. Therefore, we define a homogeneous system to illustrate the Ostwald ripening process while preserving the key characteristics of the problem in a heterogeneous system.

The system is a one-dimensional homogeneous porous medium with length L with two closed boundaries. The initial condition is that the CO_2 saturation is non-zero in the left half of the system and 0 in the right half. The mass fraction in the aqueous phase in the right half of the system is set such that any increase in CO_2 will result in the formation of separate-phase CO_2. On the left-hand side, the separate-phase CO_2 is at the residual saturation and kept immobile over the entire evolution. Over time, CO_2 will diffuse from the left domain to the right through the aqueous phase, and CO_2 saturation in the two domains will approach the same value. The entire system shares the identical capillary pressure curve so that the equivalent diffusion coefficient is continuous. In figure 4 we illustrate the defined system at its initial condition and equilibrium state.

To solve (3.7) and (3.8) for the above system, it is necessary to find a specific form of R_{CO_2}. Firstly, the derivative $\mathrm{d}P_c/\mathrm{d}X$ can be estimated from the equation-of-state for the CO_2–water–NaCl system for each temperature and pressure. For example, it can be estimated from the tangent of the molar fraction-pressure curves at a temperature and near the reservoir pressure in figure 2 of Spycher & Pruess (2005). To make the estimation more convenient, the tangent can be linked to the reservoir condition. Define

$$H_0 = \frac{P_w}{X_0}, \tag{4.1}$$

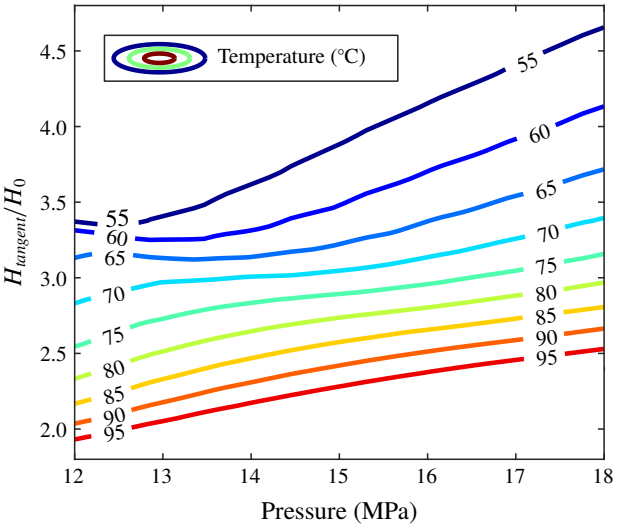

FIGURE 5. Values of $H_{tangent}/H_0$ between 12 and 18 MPa and 55 and 95 °C.

$$H_{tangent} = \frac{\mathrm{d}P_c}{\mathrm{d}X}, \tag{4.2}$$

where X_0 denotes the background saturated CO_2 mass fraction. The derivative can be expressed by the reservoir condition through

$$\frac{\mathrm{d}P_c}{\mathrm{d}X} = \frac{P_w}{X_0}\frac{H_{tangent}}{H_0}. \tag{4.3}$$

The values of the ratio $H_{tangent}/H_0$ can be found by interpolating figure 5 within a range of typical reservoir conditions for CO_2 sequestration. These values are generated by the equation-of-state ECO2N developed by Spycher & Pruess (2005).

Secondly, the derivative $\mathrm{d}S_g/\mathrm{d}P_c$ can be found by assigning a specific form for the capillary pressure model, for example,

$$P_c = a + bS_g^c, \quad a \geqslant 0,\ b \neq 0,\ c \geqslant 1, \tag{4.4}$$

where a, b and c are constants. The term $\mathrm{d}S_g/\mathrm{d}P_c$ can be written as

$$\frac{\mathrm{d}S_g}{\mathrm{d}P_c} = \frac{1}{bc}S_g^{1-c}. \tag{4.5}$$

The retardation factor can be written as

$$R_{CO_2} = 1 + \frac{\rho_g}{\rho_w}\frac{P_w}{X_0}\frac{H_{tangent}}{H_0}\frac{1}{bc}S_g^{1-c}. \tag{4.6}$$

Here, we consider a special case where $c = 1$. The capillary pressure model becomes linear. The retardation factor becomes

$$R_{CO_2} = 1 + \frac{\rho_g}{\rho_w}\frac{P_w}{X_0}\frac{H_{tangent}}{H_0}\frac{1}{b}, \tag{4.7}$$

and the equivalent diffusion coefficient becomes a constant, i.e.

$$D_{equiv} = \frac{D_w}{1 + \dfrac{\rho_g}{\rho_w}\dfrac{P_w}{X_0}\dfrac{H_{tangent}}{H_0}\dfrac{1}{b}}. \tag{4.8}$$

The boundary conditions and initial conditions are defined as

$$\frac{\partial X}{\partial x}\left(x = -\frac{L}{2}, t\right) = 0, \tag{4.9}$$

$$\frac{\partial X}{\partial x}\left(x = \frac{L}{2}, t\right) = 0, \tag{4.10}$$

$$X\left(-\frac{L}{2} < x \leqslant 0, t = 0\right) = X_1, \tag{4.11}$$

$$X\left(0 < x \leqslant \frac{L}{2}, t = 0\right) = X_0, \tag{4.12}$$

where X_1 is the saturated CO_2 mass fraction at $P_w + P_{c_1}$, with the subscript 1 denoting the domain where the initial CO_2 saturation is non-zero. The exact solution to (3.7) is given by equation (2.17) in Crank (1975):

$$X(x, t) - X_0 = \frac{1}{2}(X_{c1} - X_0)\sum_{n=-\infty}^{\infty}\left\{erf\frac{L/2 + 2nL - x}{2\sqrt{D_{equiv}t}} + erf\frac{L/2 - 2nL + x}{2\sqrt{D_{equiv}t}}\right\}. \tag{4.13}$$

The CO_2 saturation can be computed by combining (3.4) and (4.5),

$$S_g = \frac{\mathrm{d}P_c}{\mathrm{d}X}\frac{X - X_0}{b}. \tag{4.14}$$

In figure 6 we compare the exact solution with detailed numerical simulation of an example homogeneous case. The results of the numerical solution achieve a close agreement with the exact solution. The slight deviation may result from the nonlinearity of the capillary pressure–CO_2 mass fraction relationship and pressure redistribution during the evolution. The time scale of equilibration is over ten years.

4.2. *Characteristic time of Ostwald ripening*

The characteristic times of a single-phase diffusion problem and a two-phase diffusion problem discussed above are

$$t_{c,single\text{-}phase} = \frac{l^2}{D_w}, \tag{4.15}$$

$$t_{c,two\text{-}phase} = \frac{l^2}{D_{equiv}}. \tag{4.16}$$

Combining (3.8), the characteristic time of a two-phase diffusion problem (the aqueous phase and the CO_2 phase) can be expressed as

$$t_{c,two\text{-}phase} = R_{CO_2} t_{c,single\text{-}phase}. \tag{4.17}$$

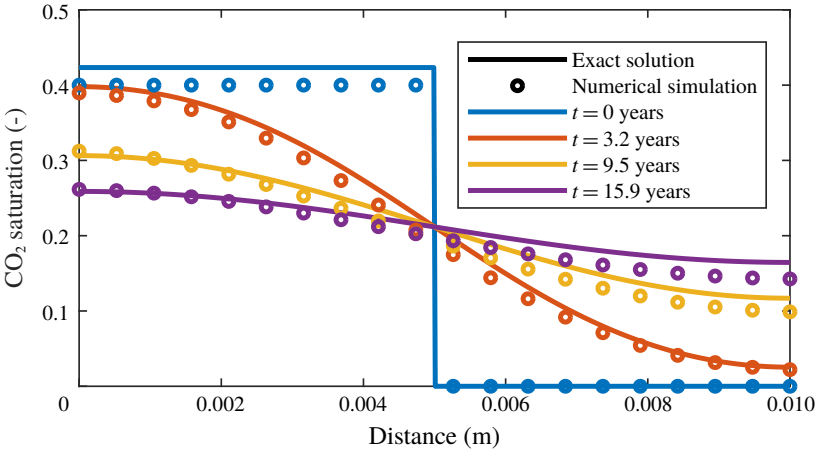

FIGURE 6. The comparison of the exact solution and detailed numerical simulation on an homogeneous case. The two results achieve close agreement. The reservoir condition is at 15 MPa and 75 °C. The initial CO_2 saturation is 0.4 in the left half of the system. The capillary pressure model is $P_c = 3000S_g$.

Therefore, it is meaningful to figure out the order of magnitude of the retardation factor as shown in (4.7) to evaluate how the characteristic time changes when the separate-phase CO_2 is involved. Firstly, the term ρ_g/ρ_w is typically on the order of 10^{-1}, where the CO_2 density is about several hundred kg m^{-3} and the water density is about 1000 kg m^{-3} at reservoir conditions. Secondly, the term P_w/X_0 is of the order of 10^9, where reservoir pressure P_w is of the order of 10^7 Pa and the CO_2 solubility in mass fraction X_0 is of the order of 10^{-2}. Thirdly, the term $H_{tangent}/H_0$ is of the order of 1 at reservoir conditions according to figure 5. Finally, the term $1/b$ is of the order of 10^{-3}, where the capillary pressure values of sandstone typical for CO_2 sequestration is about several thousand Pascal when CO_2 saturation is close to residual saturation (Krevor *et al.* 2012). Integrating all the above terms, the order of magnitude of the retardation factor is

$$R_{CO_2} \sim (1 + 10^{-1} \times 10^9 \times 1 \times 10^{-3}) \sim 10^5. \tag{4.18}$$

The large value for the retardation factor indicates that the existence of separate-phase CO_2 significantly slows down the equilibration process, compared to single-phase problems. For example, taking the characteristic length of the heterogeneous system shown in figure 3 (0.005 m), the resulting characteristic time of a single-phase diffusion problem is 4600 s, which is around an hour. However, the characteristic time for the two-phase diffusion problem is increased by 10^5, which is around 15 years. This estimation also agrees closely with the homogeneous case with an exact solution shown in figure 6. In general, CO_2 redistribution by Ostwald ripening can be expected to be a very slow process for typical reservoir properties.

5. Approximate solution for time scale estimation of residual CO_2 redistribution by Ostwald ripening in heterogeneous systems

The above sections discuss the mathematical model for residual CO_2 redistribution by Ostwald ripening and the exact solution for a homogeneous system. In more

general cases, the system is highly likely to be heterogeneous where the two adjacent domains are characterized by different capillary pressure curves. In this section, an approximate solution to estimate the time scale for Ostwald ripening is developed for heterogeneous systems.

5.1. *Derivation of the approximate solution*

The diffusive flux of CO_2 in the aqueous phase J can be written as

$$J = -\rho_w D_w \frac{\partial X}{\partial x}. \tag{5.1}$$

Assuming that the diffusion equation can be approximated by a step function at the interface between the two domains, the CO_2 diffusive flux becomes

$$J_{2\to 1} = \rho_w D_w \frac{X_2 - X_1}{\alpha L}, \tag{5.2}$$

where α is a scaling factor of the characteristic length L with its value varying during equilibration. The term α will be further defined in the next subsection. The subscripts 1 and 2 refer to the low capillary pressure domain and the high capillary pressure domains, respectively. This notation will be used throughout the derivation. The assumption of a step function achieves a first-order accuracy on predicting the diffusive flux. Since the main purpose of the approximate solution is to track the progress towards equilibrium between the two domains instead of capturing the accurate CO_2 saturation profile, this assumption is sufficient to serve such a purpose with reduced complexity.

The CO_2 mass conservation equation for domain 1 is given by

$$\frac{\partial (X_1 S_{w1} \rho_w \phi_1 A_c L_1)}{\partial t} + \frac{\partial (Y_1 S_{g1} \rho_g \phi_1 A_c L_1)}{\partial t} = A J_{2\to 1}, \tag{5.3}$$

where A_c is the cross-section area of the domain in the YZ plane and A is the available cross-section area open to diffusion. The term A is estimated by the harmonic mean of the two domains' initially available area,

$$A = \frac{2A_c}{\dfrac{1}{\phi_1(1 - S^{init}_{CO_2,1})} + \dfrac{1}{\phi_2(1 - S^{init}_{CO_2,2})}}, \tag{5.4}$$

where $S^{init}_{CO_2}$ is the initial CO_2 saturation.

Similar assumptions discussed in § 3 are applied to the derivation here including $Y_1 = 1$ and porosities and densities are constants. In addition, the rate of change of the CO_2 mass fraction in the aqueous phase is negligible because the supersaturation of the CO_2 mass fraction is only about 10^{-5} for such a slow process (figure 3). Combining (5.2) and (5.3) gives

$$\rho_g \phi_1 L_1 A_c \frac{\partial (S_{g1})}{\partial t} = A \rho_w D_w \frac{X_2 - X_1}{\alpha L}. \tag{5.5}$$

The term $X_2 - X_1$ can be found by applying a first-order approximation to (4.3), yielding

$$\frac{P_{c2}(S_{CO_2,2}) - P_{c1}(S_{CO_2,1})}{X_2 - X_1} = \frac{P_w}{X_0} \frac{H_{tangent}}{H_0}. \tag{5.6}$$

Here, the capillary pressures P_{c1} and P_{c2} are functions of $S_{CO_2,2}$ and $S_{CO_2,1}$, respectively. The CO_2 saturation in the two domains can be linked through a mass conservation equation by neglecting the concentration change in the aqueous phase, i.e.

$$S^{init}_{CO_2,1}\phi_1 L_1 + S^{init}_{CO_2,2}\phi_2 L_2 = S_{CO_2,1}\phi_1 L_1 + S_{CO_2,2}\phi_2 L_2. \tag{5.7}$$

This relationship holds over the course of the entire evolution. For simplicity, we choose that $L_1 = L_2 = L/2$.

Therefore, the diffusion equation is reduced by combining equations (5.4)–(5.7) to give

$$\begin{aligned}\frac{\mathrm{d}(S_{CO_2,1})}{\mathrm{d}t} = &\frac{4\rho_w D_w X_0 H_0}{\left[\dfrac{1}{\phi_1(1-S^{init}_{CO_2,1})} + \dfrac{1}{\phi_2(1-S^{init}_{CO_2,2})}\right]\rho_g\phi_1 L^2\alpha P_w H_{tangent}} \\ &\times\{P_{c2}(S_{CO_2,2}(S_{CO_2,1})) - P_{c1}(S_{CO_2,1})\}.\end{aligned} \tag{5.8}$$

Finally, the equation can be solved by integrating (5.8) from the initial CO_2 to any CO_2 saturation $S^*_{CO_2,1}$ before equilibrium is achieved, i.e.

$$\begin{aligned}t = &\frac{\left[\dfrac{1}{\phi_1(1-S^{init}_{CO_2,1})} + \dfrac{1}{\phi_2(1-S^{init}_{CO_2,2})}\right]\rho_g\phi_1 L^2\alpha P_w H_{tangent}}{4\rho_w D_w X_0 H_0} \\ &\times \int_{S^{init}_{CO_2,1}}^{S^*_{CO_2,1}} \frac{1}{P_{c2}(S_{CO_2,2}(S_{CO_2,1})) - P_{c1}(S_{CO_2,1})} d(S_{CO_2,1}).\end{aligned} \tag{5.9}$$

Equation (5.9) is a complete form of the approximate solution. It predicts the time required for the CO_2 saturation in domain 1 to evolve from $S^{init}_{CO_2,1}$ to $S^*_{CO_2,1}$ when the initial conditions and reservoir properties are known. The integration part in (5.9) can be solved by numerical integration or Taylor series. A complete form of the approximate solution by Taylor series is shown in (A 15) of appendix A. The value for the scaling factor α is determined by simulation results in the following subsection.

5.2. *Values of length scaling factor* α

Although the initial and equilibrated CO_2 saturation may vary from case to case over a wide range, all cases exhibit the same trend, that is, the capillary pressure gradient between the two domains declines from the initial value to zero. We define a term F to represent the remaining fraction of the driving force, e.g. capillary pressure gradient, during equilibration as follows:

$$F = \frac{P_{c2}(t) - P_{c1}(t)}{P^{init}_{c2} - P^{init}_{c2}}. \tag{5.10}$$

Here, P^{init}_c is the initial capillary pressure in each domain and $P_c(t)$ is the capillary pressure at an arbitrary time t during equilibration. The term F represents the remaining capillary pressure gradient normalized by its initial gradient. It is an indication of the progress of the equilibration by demonstrating the decline of the driving force of Ostwald ripening. The value of F is 1 at the beginning of the evolution and declines over time to 0 at equilibrium.

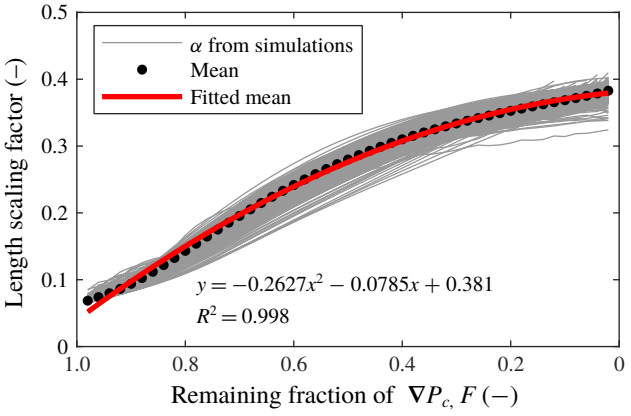

FIGURE 7. Values of α as a function of F. A total of 1000 simulations with 16 grid cells are summarized. A second-order polynomial function is fitted to the mean of α.

The value of α varies throughout the process of equilibration, and, thus, the scaled length αL that the capillary pressure difference applies to varies over time. As can be observed in the numerical solutions shown in figures 3 and 6, the capillary pressure gradient is sharp at the boundary between the two domains at the early stages of equilibration, leading to a strong diffusive flux. At later stages, the capillary pressure gradient smears out as the capillary pressure becomes more uniform within each domain. Therefore, the parameter α is adjusted to correct the diffusion length to take into consideration the strong diffusive flux at the early stages of equilibration.

Numerical simulation with various resolutions is performed to find a functional form for α. A thousand cases with randomly sampled physical parameters are run with 2 grid cells and 16 grid cells respectively. The two-grid-cell cases correspond to the assumption of step function with no spatial variation within each domain and the 16-grid-cell cases correspond to cases with spatially resolved gradients. The value of α can be found by numerical simulation based on the equation

$$\alpha(F) = \frac{t_{16-grid-cell}(F)}{t_{2-grid-cell}(F)} \times 0.5, \tag{5.11}$$

where $t_{16-grid-cell}(F)$ and $t_{2-grid-cell}(F)$ are the times required by a 2-grid-cell case and a 16-grid-cell case to evolve to a certain F. The number 0.5 denotes that the 2-grid-cell case takes the diffusion length to be $0.5L$. Here, α is a function of F that varies at different stages during equilibration.

In figure 7 we summarize α from the 1000 cases as a function of F. The value of α starts out smaller than 0.5 and increases as the system evolves towards equilibrium. A fitted mean of α is shown figure 7.

The capillary pressure gradient decline curves over time for the example case listed in table 1 are shown in figure 8. As shown in figure 8(a), grid sensitivity simulations indicate that the capillary pressure gradient declines faster in models with higher resolution. This is consistent with the fact that the capillary pressure gradient is initially very steep between the two domains. In figure 8(b) we show the capillary pressure decline curve predicted by the approximate solution with and without the corrected diffusion length by α. Without the correction ($\alpha = 0.5$), the prediction of

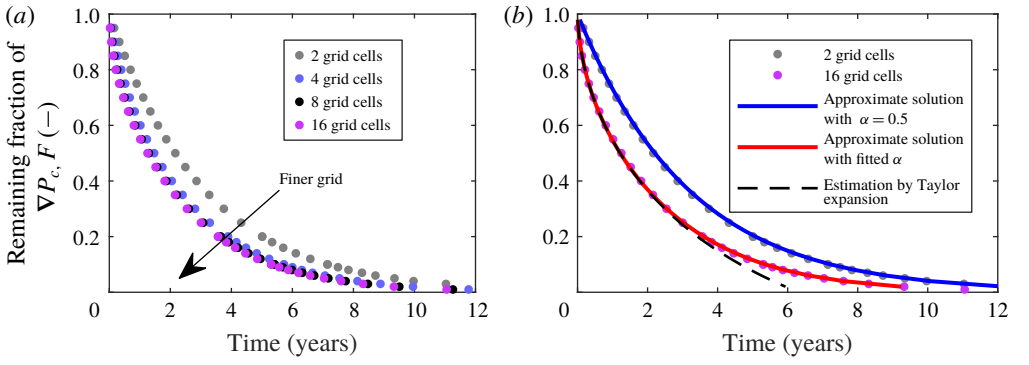

FIGURE 8. Capillary pressure decline curves of the example case shown in figure 3.

Category	Parameter	Lower bound	Upper bound	Unit	Description
Rock property	k	1	1000	mD	Permeability
	ϕ	0.02	0.31	—	Porosity
Capillary pressure model	P_e	100	25 000	Pa	Entry pressure
	P_0	100	30 000	Pa	Fitting parameter 1
	λ	0.4	0.99	—	Fitting parameter 2
	S_{wi}	0	0.3	—	Irreducible water
Model size	L	0.001	1	m	Size of the entire model
Initial condition	P_w	12	18	MPa	Reservoir pressure
	$S_{CO_2}^{init}$	0.1	0.4	—	Initial CO_2 saturation
	T	55	95	°C	Temperature
	D_w	4×10^{-9}	7×10^{-9}	$m^2\ s^{-1}$	Diffusion coefficient of CO_2 in the aqueous phase (Cadogan *et al.* (2014))

TABLE 2. Numerical simulation input parameters and ranges for sampling.

the approximate solution agrees well with the numerical solutions with two grid cells, corresponding to the assumption of step function. With correction by fitted mean of α, the approximate solution captures the time-varying diffusion length and, thus, achieves an excellent agreement with the numerical simulation with high resolution.

5.3. *Validation of the approximate solution*

The approximate solution is validated through comparison with detailed numerical simulations. To test the robustness of the solution, each physical parameter of a single case is randomly sampled from a wide range that is representative of geological CO_2 storage parameters, as shown in table 2. Correlations of key physical parameters are shown in figure 9. A total of 1000 simulations are performed.

In figure 10(*a*) we compare the simulation results from 1000 randomly sampled cases (performed with 16 grid cells) with predictions from the approximate solution at various values of F. The agreement is excellent at both early and late stages of evolution. Errors are measured by the difference of capillary pressure decline curves predicted by the approximate solution and numerical simulation in both the horizontal

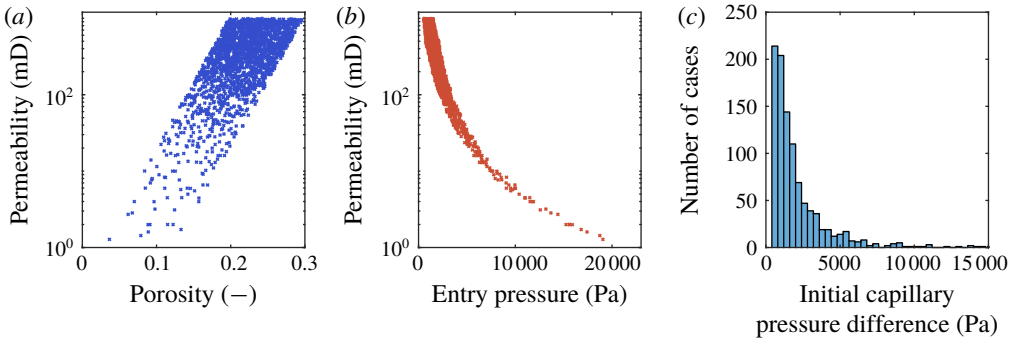

FIGURE 9. Input parameters and correlations for the 1000 runs used to test the approximate solution. (*a*) Porosity and permeability are positively correlated. (*b*) Entry pressure and permeability are negatively correlated. (*c*) The majority of cases have initial capillary pressure differences below 5000 Pa.

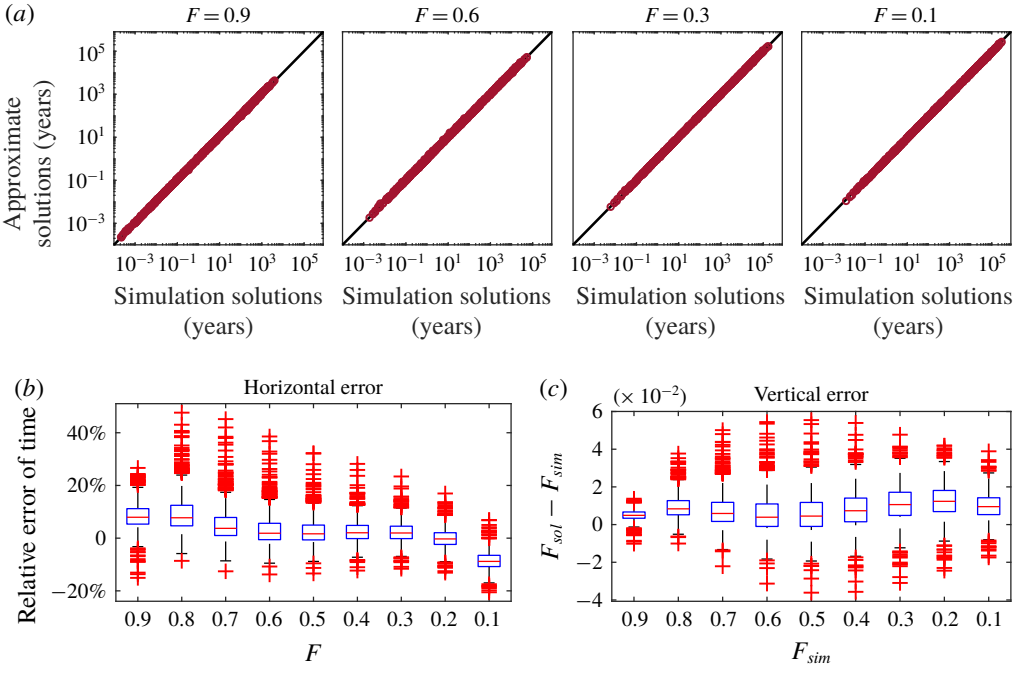

FIGURE 10. (*a*) The comparison of evolution time between numerical simulations with 16 grid cells and predictions by the approximate solution (5.9). The agreement is fairly close. (*b*) The relative error of time for the system to evolve to a range of F values. (*c*) The error of F values predicted by the approximate solution and numerical simulation measured at a range of F from numerical simulation.

and vertical directions. In figure 10(*b*) we measure the horizontal difference, which is the relative error of time for the system to evolve to a range of F values. In figure 10(*c*) we measure the vertical difference, which is the difference between F predicted by the solution and numerical simulation. The lower and upper quartile of

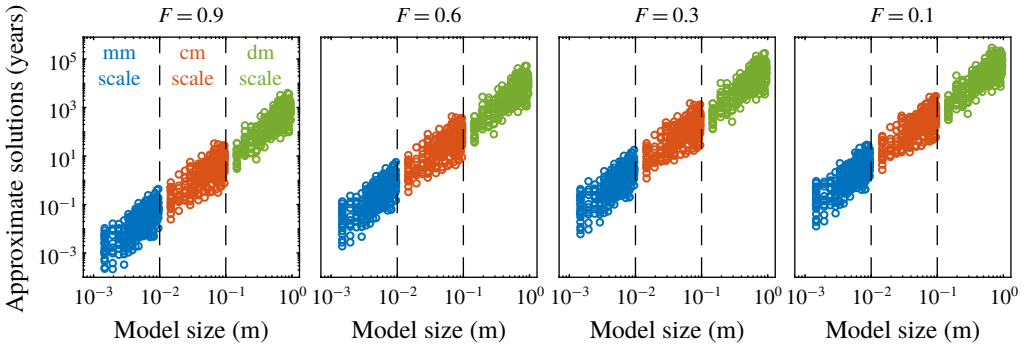

FIGURE 11. The time scale of residual CO_2 redistribution by Ostwald ripening within a range of model sizes at selected F values. The results are predicted by the approximate solution and validated by numerical simulation. The time scale of redistribution increases with the increase of model size ($\sim L^2$). For example, millimetre-scale models may have an evolution time scale ranging from months to years. Models over metre scales may take thousands of years or longer to equilibrate.

both errors are within ± 0.02, indicating that the approximate solution achieves a close agreement with numerical simulation.

6. Discussion

6.1. *Implications for the long-term fate of residual* CO_2

We have demonstrated and quantified the time scale for a new mechanism for redistribution of residually trapped CO_2 due to reservoir heterogeneity. The CO_2 saturations will increase in portions of the rocks with lower capillary pressure and decrease in those with higher capillary pressures. Such are the conditions expected to be present after imbibition of reservoir brine into the CO_2 plume during the post-injection period. As shown in figure 11, for millimeter-scale systems, the time scale of mass redistribution ranges from days to years, varying by several orders of magnitude depending on the total mass of CO_2, capillary heterogeneity and reservoir conditions. The time scale increases with the increase of model size L following a power law ($\sim L^2$), such that a metre-scale model may take thousands of years or more to redistribute residually trapped CO_2.

The time period for continuum-scale Ostwald ripening depends on the nature of the capillary pressure curves during redistribution of the CO_2. We have assumed particular parametric forms for these curves, based on a plausible understanding of the pore-scale processes that are occurring. To date, there are no direct measurements of the capillary pressure curves during Ostwald ripening. It would be valuable to make these measurements to include them in model calculations. This would be a challenging but worthwhile pursuit, ideally done by combining both pore-scale and continuum-scale measurements. In addition, we assume that the relative permeability to CO_2 phase is zero for all times and throughout both domains. For the domain with increasing saturations, it is certainly possible that the CO_2 phase would become mobile. If this occurs, we would expect that Ostwald ripening would be slightly faster, due to the redistribution of CO_2 away from the interface between the two domains.

This study seeks to evaluate the impact of Ostwald ripening on trapped CO_2, and, thus, geological gradients other than the capillary pressure gradient such

as pressure gradients by regional flow and other potential mechanisms of mass transfer in a geological storage site are neglected. In reality, other processes such as brine advection, CO_2 dissolution and mineralization will take place simultaneously. For example, advection and buoyancy-driven flows may increase the risk of remobilization of aggregated CO_2, while dissolution of trapped CO_2 may mitigate CO_2 aggregation by reducing the total amount of residually trapped CO_2. Coupling of these mechanisms would be another interesting topic that may affect the fate of trapped CO_2 significantly.

While this study has focused on the CO_2–water system, it is equally applicable to other systems where the non-wetting phase is soluble in the wetting phase, for example, the methane–brine system. Hydrocarbon migration takes place on similar time scales to the processes described here, suggesting that Ostwald ripening due to reservoir heterogeneity may play a role in basin-scale gas migration.

6.2. *Trend of capillary pressure of a shrinking* CO_2 *ganglion*

The approximate solution and numerical simulation are developed with a monotonically decreasing capillary pressure model by assuming that the residual CO_2 always attaches to the pore matrix during equilibration. It is likely that at some point, the CO_2 ganglion will become smaller than the pore body, no longer being supported by the pore walls. Once this occurs, the structure of the porous media no longer controls the capillary pressure because the ganglion will become a spherical bubble, resulting in an increase in curvature. At this point, as ripening proceeds, the capillary pressure will progressively increase as the bubble shrinks and disappears. In figure 12 we present a conceptual illustration of capillary pressure of a trapped ganglion including ganglion detachment from the pore walls. A minimum capillary pressure could exist near the saturation where detachment of ganglia may happen.

Some previous works have focused on exploring the impact on capillary pressure by the residual portion of the non-wetting phase by pore-network modelling. Conventionally, the capillary pressure curve constructed by experiments is only between the wetting phase and the continuous portion of the non-wetting phase, and the residual portion of the non-wetting phase is excluded from the measurement (Bear 2013). McClure *et al.* (2016) showed that the capillary pressure within a porous medium increases with an increasing number of ganglia and decreasing non-wetting phase saturation near low non-wetting phase saturations, resulting from detachment of non-wetting phase ganglia detachment from the pore walls. de Chalendar *et al.* (2018) showed that the trend of capillary pressure of a single ganglion is opposite before and after detachment. These works imply that the trend of capillary pressure of the residual non-wetting phase could be altered due to ganglion detachment from the pore walls when the non-wetting phase saturation is small.

Our mathematical model does not explicitly include this last stage because it will be relevant only for scenarios where the non-wetting phase completely disappears from one of the domains. Even so, the consequence of excluding it will be that Ostwald ripening occurs faster than we predict in these late stages. In figure 13 we show three possible equilibrium states considering the upward trend of capillary pressure curves at low CO_2 saturations. For this study, we assume that the initial condition for Ostwald ripening is at the end of imbibition and that all of the CO_2 ganglia are supported by pore walls. The equilibrium state is determined by both capillary pressure and mass conservation. Equilibrium state 1 corresponds to the case discussed in the approximate solution that the capillary pressures of the two domains reach equilibrium without

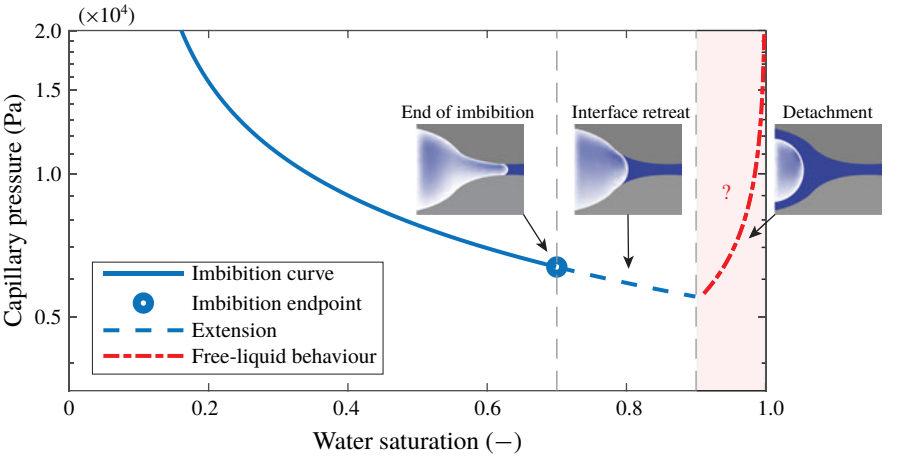

FIGURE 12. A conceptual description of a capillary pressure curve for a shrinking ganglion due to Ostwald ripening. At the endpoint of the imbibition capillary pressure curve, the ganglion is trapped in the pore space with its interface extended into the pore throat. For regions where the CO_2 saturation is decreasing, as Ostwald ripening progresses, the interface of the ganglion retreats from the pore throat towards the pore body. At some point, the ganglion may shrink and retreat fully into the pore body. Once the ganglion separates from the pore wall, we assume that since the rock is water-wet, the curvature corresponds to the radius of a spherical bubble and increases rapidly as the bubble shrinks and eventually disappears. The precise nature of the capillary pressure curve at this time is unknown, and the representation is provided here only for illustrative purposes. The rising trend of capillary pressure after ganglion detachment are illustrated in de Chalendar *et al.* (2018) and McClure *et al.* (2016).

any detachment. At equilibrium state 2, the capillary pressures reach equilibrium with the capillary pressure of one side going over the minimum value. At equilibrium state 3, the capillary pressure of the CO_2-discharging domain increases rapidly after detachment until separate-phase CO_2 is depleted.

In figure 13 we also show the evolution of the remaining driving force for Ostwald ripening during equilibration. At equilibrium state 2, it indicates that the ganglia in one domain are no longer supported by pore walls, but it is still possible for the capillary pressures of the two domains to approach the same value. Because the diffusive flux of CO_2 is always from the high capillary pressure domain to the low capillary pressure domain, Ostwald ripening will still progress in the same direction as long as the direction of the capillary pressure gradient remains the same. At equilibrium state 3, after the capillary pressure of the high capillary pressure domain passes the minimum value, the capillary pressure gradient progressively increases in the same direction, which can accelerate diffusive transport between the two domains. The gradient may keep increasing until all of the separate-phase CO_2 is transported to the low capillary pressure domain. Therefore, Ostwald ripening can still progress in the same direction taking into consideration the detachment from the pore wall of shrinking ganglia and even be faster than predicted by the approximate solution due to increasing capillary pressure gradients. However, when and how the detachment of ganglia happen by Ostwald ripening in real-rock systems and how much Ostwald ripening can be accelerated is also an interesting research question to be explored further.

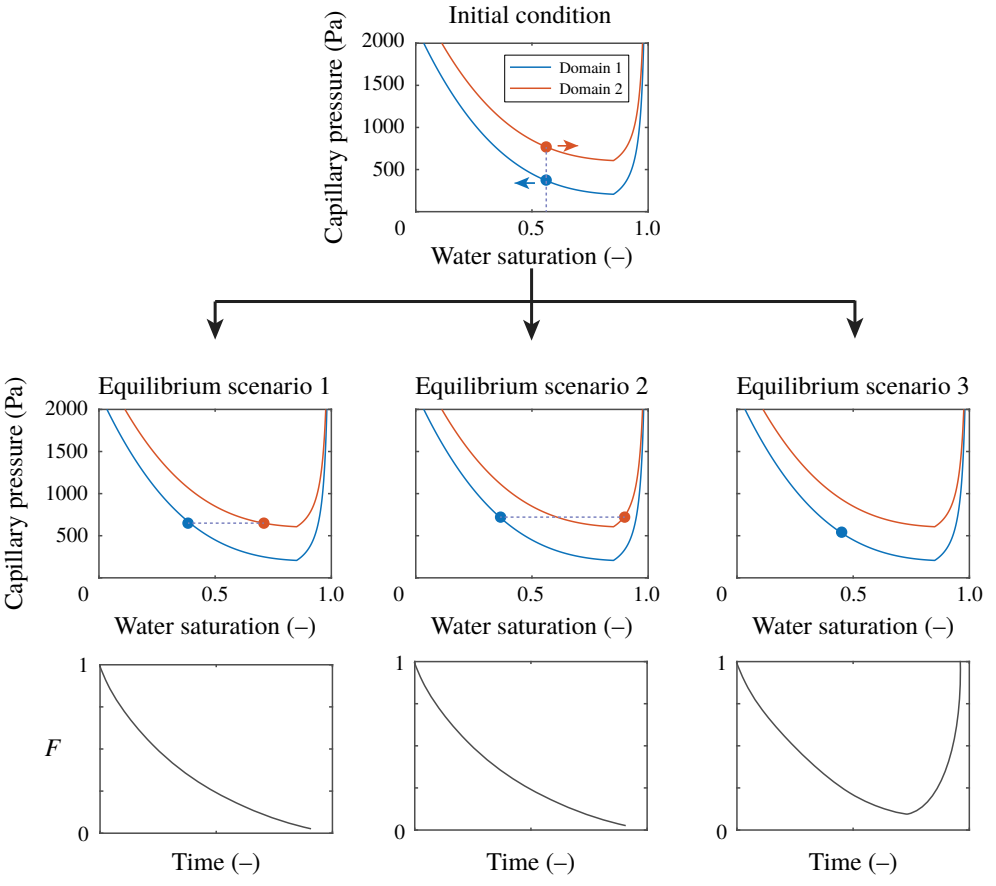

FIGURE 13. Examples of possible equilibrium states of Ostwald ripening based on capillary pressure curves with a rising trend near low CO_2 saturation. The equilibrium state is determined by both capillary pressure curves and CO_2 mass conservation. Scenario 1: equilibrium at equal capillary pressure. Scenario 2: equilibrium at equal capillary pressure with one domain passing the minimum capillary pressure. Scenario 3: all of the separate-phase CO_2 in one domain is transported to the other.

7. Conclusions

This study proposed and investigated a new mechanism for mass redistribution of residually trapped supercritical CO_2 within porous media with capillary heterogeneity. A new conceptual model, numerical simulation, and a new approximate solution were developed to demonstrate that Ostwald ripening, a pore-scale phenomenon, can result in continuum-scale redistribution of trapped CO_2. Increases in CO_2 saturation could potentially lead to remobilization of residually trapped CO_2.

An analogous retardation factor is derived to illustrate that the characteristic time for Ostwald ripening is of the order of 10^5 times slower than a single-phase diffusion problem due to the existence of separate-phase CO_2. An approximate solution for predicting the time scale of the mass redistribution due to Ostwald ripening was developed and validated through numerical simulation over a wide range of parameters that covered typical conditions for a geological storage site. Results showed that for millimetre-scale spatial domains, redistribution and capillary equilibration can occur

on the time scale of months to years. For metre-scale systems, redistribution is very slow, requiring 10 000 years and longer. Although CO_2 redistribution by Ostwald ripening is a fairly slow process and seems to have little impact at the reservoir scale, at small spatial scales it can occur quickly. Understanding the implications of this process on long-term plume evolution will require consideration of the complex interplay of viscous, buoyancy and capillary forces, along with dissolution of the CO_2 into reservoir brine due to convective mixing or regional groundwater flow.

Acknowledgements

This study was funded by the Global Climate and Energy Project. We thank faculty members and students in the Department of Energy Resources Engineering for inspiring discussions and thoughtful opinions.

Declaration of interests

The authors report no conflict of interest.

Appendix A

To solve the integration part of the approximate solution, Taylor series can be applied to achieve a close estimation. The integration part of the approximate solution is

$$\int_{S^{init}_{CO_2,1}}^{S^{*}_{CO_2,1}} \frac{1}{P_{c2}(S_{CO_2,2}) - P_{c1}(S_{CO_2,1})} d(S_{CO_2,1}). \tag{A 1}$$

Define

$$f(S_{CO_2,1}) = \frac{1}{P_{c2}(S_{CO_2,2}) - P_{c1}(S_{CO_2,1})}. \tag{A 2}$$

Capillary pressure is represented by

$$P_{c1} = P_{e1} + P_{01}\left(\frac{1 - S_{wi,1}}{S_{CO_2,1}} - 1\right)^{-(1/\lambda_1)} \tag{A 3}$$

and

$$P_{c2} = P_{e2} + P_{02}\left(\frac{1 - S_{wi,2}}{S_{CO_2,2}} - 1\right)^{-(1/\lambda_2)}. \tag{A 4}$$

The relationship of $S_{CO_2,1}$ and $S_{CO_2,2}$ can be acquired from (5.7) as follows:

$$S_{CO_2,2} = aS_{CO_2,1} + b. \tag{A 5}$$

Here,

$$a = -\frac{\phi_1}{\phi_2} \tag{A 6}$$

and

$$b = \frac{\phi_1}{\phi_2} S^{init}_{CO_2,1} + S^{init}_{CO_2,2}. \tag{A 7}$$

Therefore, (A 2) can be written as

$$f(S_{CO_2,1}) = \frac{1}{P_{e2} + P_{02}\left(\dfrac{1-S_{wi,2}}{aS_{CO_2,1}+b} - 1\right)^{-(1/\lambda_2)} - P_{e1} - P_{01}\left(\dfrac{1-S_{wi,1}}{S_{CO_2,1}} - 1\right)^{-(1/\lambda_1)}}. \tag{A 8}$$

Writing (A 8) in the form of a Taylor series evaluated at S_0, we obtain

$$f(S_{CO_2,1}) = f(S_0) + f'(S_0)(S_{CO_2,1} - S_0) + \frac{f''(S_0)}{2}(S_{CO_2,1} - S_0)^2, \tag{A 9}$$

where

$$S_0 = 0.5(S^{init}_{CO_2,1} + S^{eq}_{CO_2,1}). \tag{A 10}$$

The term $S^{eq}_{CO_2,1}$ can be solved by equating the right-hand side of (A 3) and (A 4) and combining (5.7).

Write out the three terms about $f(S_0)$:

$$f(S_0) = \frac{1}{P_{e2} + P_{02}\left(\dfrac{1-S_{wi,2}}{aS_0+b} - 1\right)^{-(1/\lambda_2)} - P_{e1} - P_{01}\left(\dfrac{1-S_{wi,1}}{S_0} - 1\right)^{-(1/\lambda_1)}}, \tag{A 11}$$

$$f'(S_0) = -[f(S_0)]^2\left[\frac{aP_{02}(1-S_{wi,2})}{\lambda_2(aS_0+b)^2}\left(\frac{1-S_{wi,2}}{aS_0+b} - 1\right)^{-(1/\lambda_2)-1} - \frac{P_{01}(1-S_{wi,1})}{\lambda_1 S_0^2}\left(\frac{1-S_{wi,1}}{S_0} - 1\right)^{-(1/\lambda_1)-1}\right], \tag{A 12}$$

$$\begin{aligned} f''(S_0) = {} & \frac{2[f'(S_0)]^2}{f(S_0)} - [f(S_0)]^2\left[-\frac{2a^2P_{02}(1-S_{wi,2})}{\lambda_2(aS_0+b)^3}\left(\frac{1-S_{wi,2}}{aS_0+b} - 1\right)^{-(1/\lambda_2)-1}\right. \\ & + \frac{a^2P_{02}(1-S_{wi,2})^2(1+\lambda_2)}{\lambda_2^2(aS_0+b)^4}\left(\frac{1-S_{wi,2}}{aS_0+b} - 1\right)^{-(1/\lambda_2)-2} \\ & + \frac{2P_{01}(1-S_{wi,1})}{\lambda_1 S_0^3}\left(\frac{1-S_{wi,1}}{S_0} - 1\right)^{-(1/\lambda_1)-1} \\ & \left. - \frac{(1-S_{wi,1})^2P_{01}(1+\lambda_1)}{\lambda_1^2 S_0^4}\left(\frac{1-S_{wi,1}}{S_0} - 1\right)^{-(1/\lambda_1)-2}\right]. \end{aligned} \tag{A 13}$$

Therefore, the integration can be written in the following form:

$$\begin{aligned} & \int_{S^{init}_{CO_2,1}}^{S^{*}_{CO_2,1}} \frac{1}{P_{c2}(S_{CO_2,2}) - P_{c1}(S_{CO_2,1})} d(S_{CO_2,1}) \\ & = \int_{S^{init}_{CO_2,1}}^{S^{*}_{CO_2,1}} f(S_{CO_2,1}) d(S_{CO_2,1}) \\ & = \left[f(S_0)S_{CO_2,1} + f'(S_0)\left(\frac{1}{2}S^2_{CO_2,1} - S_0 S_{CO_2,1}\right)\right. \end{aligned}$$

$$+\frac{f''(S_0)}{2}\left(\frac{1}{3}S_{CO_2,1}^3 - S_0 S_{CO_2,1}^2 + S_0^2 S_{CO_2,1}\right)\Bigg]\Bigg|_{S_{CO_2,1}^{init}}^{S_{CO_2,1}^*}$$

$$= \left[f(S_0)S_{CO_2,1}^* + f'(S_0)\left(\frac{1}{2}S_{CO_2,1}^{*2} - S_0 S_{CO_2,1}^*\right)\right.$$

$$\left. + \frac{f''(S_0)}{2}\left(\frac{1}{3}S_{CO_2,1}^{*3} - S_0 S_{CO_2,1}^{*2} + S_0^2 S_{CO_2,1}^*\right)\right]$$

$$- \left[f(S_0)S_{CO_2,1}^{init} + f'(S_0)\left(\frac{1}{2}S_{CO_2,1}^{init2} - S_0 S_{CO_2,1}^{init}\right)\right.$$

$$\left. + \frac{f''(S_0)}{2}\left(\frac{1}{3}S_{CO_2,1}^{init3} - S_0 S_{CO_2,1}^{init2} + S_0^2 S_{CO_2,1}^{init}\right)\right]. \tag{A 14}$$

To summarize, the complete form of the approximate solution by Taylor series evaluated at $S_0 = 0.5(S_{CO_2,1}^{init} + S_{CO_2,1}^{eq})$ is

$$t = \frac{\left[\frac{1}{\phi_1(1 - S_{CO_2,1}^{init})} + \frac{1}{\phi_2(1 - S_{CO_2,2}^{init})}\right]\rho_g \phi_1 L^2 \alpha P_w H_{tangent}}{4\rho_w D_w X_0 H_0}$$

$$\times \left\{\left[f(S_0)S_{CO_2,1}^* + f'(S_0)\left(\frac{1}{2}S_{CO_2,1}^{*2} - S_0 S_{CO_2,1}^*\right)\right.\right.$$

$$\left. + \frac{f''(S_0)}{2}\left(\frac{1}{3}S_{CO_2,1}^{*3} - S_0 S_{CO_2,1}^{*2} + S_0^2 S_{CO_2,1}^*\right)\right]$$

$$- \left[f(S_0)S_{CO_2,1}^{init} + f'(S_0)\left(\frac{1}{2}S_{CO_2,1}^{init2} - S_0 S_{CO_2,1}^{init}\right)\right.$$

$$\left.\left. + \frac{f''(S_0)}{2}\left(\frac{1}{3}S_{CO_2,1}^{init3} - S_0 S_{CO_2,1}^{init2} + S_0^2 S_{CO_2,1}^{init}\right)\right]\right\}, \tag{A 15}$$

where $f(S_0)$, $f'(S_0)$ and $f''(S_0)$ can be found using (A 11)–(A 13).

REFERENCES

ANDREW, M., BIJELJIC, B. & BLUNT, M. J. 2014 Pore-by-pore capillary pressure measurements using X-ray microtomography at reservoir conditions: curvature, snap-off, and remobilization of residual CO_2. *Water Resour. Res.* **50** (11), 8760–8774.

BEAR, J. 2013 *Dynamics of Fluids in Porous Media*. Dover Publications.

BURNSIDE, N. M. & NAYLOR, M. 2014 Review and implications of relative permeability of CO_2/brine systems and residual trapping of CO_2. *Intl J. Greenh. Gas Control* **23**, 1–11.

CADOGAN, S. P., MAITLAND, G. C. & TRUSLER, J. P. M. 2014 Diffusion coefficients of CO_2 and N_2 in water at temperatures between 298.15 K and 423.15 K at pressures up to 45 MPa. *J. Chem. Engng Data* **59** (2), 519–525.

DE CHALENDAR, J. A., GARING, C. & BENSON, S. M. 2018 Pore-scale modelling of Ostwald ripening. *J. Fluid Mech.* **835**, 363–392.

CRANK, J. 1975 *The Mathematics of Diffusion*, 2nd edn. Clarendon Press.

DOMINGUEZ, A., BORIES, S. A. & PRAT, M. 2000 Gas cluster growth by solute diffusion in porous media. Experiments and automaton simulation on pore network. *Intl J. Multiphase Flow* **26** (12), 1951–1979.

FOKAS, A. S. & YORTSOS, Y. C. 1982 On the exactly solvable equation $s_t = (\beta s + \gamma)^{-2} s_x]_x + \alpha(\beta s + \gamma)^{-2} s_x$ occurring in two-phase flow in porous media. *SIAM J. Appl. Maths* **42** (2), 318–415.

GARING, C., DE CHALENDAR, J. A., VOLTOLINI, M., AJO-FRANKLIN, J. B. & BENSON, S. M. 2017 Pore-scale capillary pressure analysis using multi-scale x-ray micromotography. *Adv. Water Resour.* **104**, 223–241.

GOLDOBIN, D. S. & BRILLIANTOV, N. V. 2011 Diffusive counter dispersion of mass in bubbly media. *Phys. Rev.* E **84**, 056328.

GREENWOOD, G. W. 1956 The growth of dispersed precipitates in solutions. *Acta Metall.* **4**, 243–248.

HESSE, M. A., ORR, F. M. & TCHELEPI, H. A. 2008 Gravity currents with residual trapping. *J. Fluid Mech.* **611**, 35–60.

KASHCHIEV, D. & FIROOZABADI, A. 2003 Analytical solutions for 1D countercurrent imbibition in water-wet media. *SPE J.* **8**, 401–408.

KREVOR, S. C. M., PINI, R., ZUO, L. & BENSON, S. M. 2012 Relative permeability and trapping of CO_2 and water in sandstone rocks at reservoir conditions. *Water Resour. Res.* **48** (2), W02532.

LI, X. & YORTSOS, Y. C. 1995 Theory of multiple bubble growth in porous media by solute diffusion. *Chem. Engng Sci.* **50** (8), 1247–1271.

LIFSHITZ, I. M. & SLYOZOV, V. V. 1961 The kinetics of precipitation from supersaturated solid solutions. *J. Phys. Chem. Solids* **19** (1-2), 35–50.

MCCLURE, J. E., BERRILL, M. A., GRAY, W. G. & MILLER, C. T. 2016 Influence of phase connectivity on the relationship among capillary pressure, fluid saturation, and interfacial area in two-fluid-phase porous medium systems. *Phys. Rev.* E **94**, 033102.

NARASIMHAN, T. N., WITHERSPOON, P. A. & EDWARDS, A. L. 1978 Numerical model for saturated–unsaturated flow in deformable porous media: 2. The algorithm. *Water Resour. Res.* **14** (2), 255–261.

PINI, R., KREVOR, S. C. M. & BENSON, S. M. 2012 Capillary pressure and heterogeneity for the CO_2/water system in sandstone rocks at reservoir conditions. *Adv. Water Resour.* **38**, 48–59.

PLESSET, M. S. & SADHAL, S. S. 1982 On the stability of gas bubbles in liquid–gas solutions. *Appl. Sci. Res.* **38** (1), 133–141.

PRUESS, K., OLDENBURG, C. & MORIDIS, G. 1999 TOUGH2 user's guide, version 2.0.

PRUESS, K. & SPYCHER, N. 2007 ECO2N – A fluid property module for the TOUGH2 code for studies of CO_2 storage in saline aquifers. *Energy Convers. Manage.* **48** (6), 1761–1767.

SPYCHER, N. & PRUESS, K. 2005 CO_2–H_2O mixtures in the geological sequestration of CO_2. II. Partitioning in chloride brines at 12 100 °C and up to 600 bar. *Geochim. Cosmochim. Acta* **69** (13), 3309–3320.

TSIMPANOGIANNIS, I. N. & YORTSOS, Y. C. 2002 Model for the gas evolution in a porous medium driven by solute diffusion. *AIChE J.* **48** (11), 2690–2710.

VAN GENUCHTEN, M. 1980 A closed-form equation for predicting the hydraulic conductivity of unsaturated soils1. *Soil Sci. Soc. Amer. J.* **44**, 892–898.

VERMA, A. K., PRUESS, K., TSANG, C. F. & WITHERSPOON, P. A. 1985 A study of two-phase concurrent flow of steam and water in an unconsolidated porous medium. In *Proceedings of the 23rd National Heat Transfer Conference, Denver, CO*, pp. 135–143. ASME.

VOORHEES, P. W. 1985 The theory of Ostwald ripening. *J. Stat. Phys.* **38** (1/2), 231–252.

VOORHEES, P. W. 1992 Ostwald ripening of two-phase mixtures. *Annu. Rev. Mater. Sci.* **22** (1), 197–215.

XU, K., BONNECAZE, R. & BALHOFF, M. 2017 Egalitarianism among bubbles in porous media: an Ostwald ripening derived anticoarsening phenomenon. *Phys. Rev. Lett.* **119**, 264502.